Supplementary Information (SI) for Journal of Materials Chemistry A.

Supporting Information

for

Electrodeposited CoP_2 on CO_2-Laser-Modified Graphite Felt: A Robust Electrocatalyst for Nitrite Reduction to Ammonia

Chae Eun Park [a,†], Rahul Kerkar [a,†], Deepak Arumugam [b,†], Jayaraman Theerthagiri [a], Shankar Ramasamy [b], Myong Yong Choi [a,c*]

[a] Department of Chemistry (BK21 FOUR), Research Institute of Advanced Chemistry, Gyeongsang National University, Jinju 52828, Republic of Korea

[b] Molecular Simulation Laboratory, Department of Physics, Bharathiar University, Coimbatore 641046, Tamil Nadu, India

[c] Core-Facility Center for Photochemistry & Nanomaterials, Gyeongsang National University, Jinju 52828, Republic of Korea

*Correspondence Email address: mychoi@gnu.ac.kr (M.Y. Choi)

[†] These authors contributed equally to this work

Characterization

A range of analytical techniques was employed to evaluate the crystallinity, morphology, elemental composition, chemical bonding, and analyte quantification of the synthesized electrocatalysts. The crystallinity and phase composition were analyzed using X-ray diffraction (XRD) with a Bruker D8 Advance A25 diffractometer equipped with a CuKα radiation source ($\lambda = 1.54$ Å). The diffraction patterns were recorded at a scan rate of 0.05° s^{-1} over a 2θ range of 20° – 60°, ensuring high-resolution phase identification. Raman spectroscopy was performed using a Thermo Scientific DXR2xi Raman imaging microscope to elucidate the structural characteristics of the catalysts. The morphology and elemental distribution were examined via field emission scanning electron microscopy (FESEM) on a TESCAN S8000 instrument, equipped with an Ultim Max energy-dispersive X-ray spectroscopy (EDS) detector (Oxford Instruments). X-ray photoelectron spectroscopy (XPS) was conducted using a Thermo Scientific Nexsa G2 instrument to determine the chemical states and bonding environment of the elements within the synthesized material. The quantification of ammonium ions (NH_4^+) was performed spectrophotometrically using a Thermo Scientific Evolution 600 UV-Vis spectrophotometer, with measurements recorded in the visible range of 400–800 nm. Additionally, ^1H NMR spectroscopy was employed for NH_4^+ quantification using a Bruker Avance-III 300 NMR spectrometer operating at 300 MHz.

Electrocatalytic Activity Study

The catalytic performance of the synthesized electrocatalysts for the nitrite reduction reaction (NO_2RR) was evaluated in a two-compartment, three-electrode electrochemical system using a CHI708E electrochemical workstation (CHI Instruments, USA). The reaction was conducted in 0.1 M KNO_2 solution, with a Nafion membrane serving as both a proton-exchange membrane and an electrolyte separator. Prior to use, the Nafion membrane was pretreated by sequential immersion in 3% H_2O_2 for 1 h, deionized water for 2 h, and 0.5 M H_2SO_4 for 1 h at 80 °C. Graphite felt modified with the electrocatalyst was employed as the working electrode, a Hg/HgO electrode was used as the reference electrode, and a graphite rod served as the counter electrode. The measured potentials were converted to the reversible hydrogen electrode (RHE) scale using the standard equation: $E_{RHE} = E_{Hg/HgO} + (0.098 + 0.0591 \times pH)$. Linear sweep voltammetry (LSV) was conducted to assess NO_2RR activity over an anodic potential range of –0.6 to –1.9 V vs. Hg/HgO, at a scan rate of 5 mV s^{-1}. The Tafel slope was determined using the equation: $\eta = b \times \log (j/j_0)$, where η represents the overpotential, b is the Tafel slope, j is the current density, and j_0 is the exchange current density. Bulk NO_2RR analysis was performed at a constant potential for 1 h in 45 mL of catholyte, with continuous stirring at 300 rpm to ensure homogeneous mixing.

Quantification of NH_4^+

Colorimetric indophenol blue method

The concentration of NH_4^+ generated during NO_2RR was determined using the colorimetric indophenol blue method, followed by UV-Vis spectrophotometric analysis. Reaction aliquots were collected at 1 h intervals, and 2 mL of the collected sample was mixed with 2 mL of 1.0 M NaOH containing 5 wt% sodium citrate ($C_6H_5Na_3O_7 \cdot 2H_2O$) and 5 wt% salicylic acid ($C_7H_6O_3$). Subsequently, 2 mL of 0.05 M NaCl and 0.2 mL of 1 wt% sodium nitroferricyanide dihydrate ($C_5H_4FeN_6Na_2O_3 \cdot 2H_2O$) were added. The solution was allowed to stand for 2 hrs to develop the characteristic indophenol blue coloration. The absorbance was measured at a wavelength of 655 nm (λ_{max}), and the NH_4^+ concentration was quantified using a calibration curve constructed from standard NH_4Cl solutions with concentrations of 0, 10, 50, 100, and 200 ppm. This method provided a reliable estimation of NH_4^+ formation during NO_2RR.

^{1}H Nuclear Magnetic Resonance (^{1}H NMR) Studies

^{1}H NMR Spectroscopy for NH_4^+ Quantification^{1}H NMR spectroscopy was employed to confirm NH_4^+ formation and to determine its concentration based on peak area integration. For NMR analysis,1 mL of the reaction solution collected after 1 h of NO_2RR was mixed with 0.5 mL of deuterium oxide (D_2O). The pH of the solution was adjusted to ~2 using 0.5 M H_2SO_4 to optimize NH_4^+ detection conditions. The ^{1}H NMR spectra exhibited three distinct peaks at $\delta = 7.25$, 6.95, and 6.65 ppm, corresponding to NH_4^+ ions. The unknown NH_4^+ concentration was determined by referencing a calibration curve generated from standard NH_4Cl solutions with concentrations of 1, 5, 10, and 20 mM (equivalent to ~18, 90, 180, and 360 ppm, respectively). This analytical approach effectively confirmed and quantified NH_4^+ formation during the catalytic NO_2RR process.

Computational Details

First-principles density functional theory (DFT) calculations were performed to investigate the NO_2RR performance of the CoP_2/GO-GF structure using the Vienna *Ab initio* Simulation Package (VASP)[1, 2]. The spin-polarized Perdew–Burke–Ernzerhof (PBE) functional, based on the generalized gradient approximation (GGA) , was employed to describe the electron–ion interactions. The electron cloud was modeled using a plane-wave basis set in conjunction with projector augmented wave (PAW) pseudopotentials [3, 4]. To account for weak interactions, Grimme's dispersion correction (D3) with Becke–Johnson damping was incorporated[5]. The convergence criteria for the electronic self-consistent field (SCF) steps and the interatomic forces were set to 10^{-6} eV and 0.01 eV/Å, respectively, for all systems. The Brillouin zone was sampled using the Monkhorst–Pack scheme with a 5 × 5 × 1 *k*-mesh and Gaussian smearing. The plane-wave expansion was confined within a cutoff energy of 520 eV [6]. For density of states (DOS) calculations, a denser 11 × 11 × 1 *k*-point grid was employed using the tetrahedron method with Blöchl corrections [7]. To prevent interactions with periodic images a vacuum separation of 30 Å was maintained in the z-direction. Additional details regarding electrochemical calculations are provided in the Supporting Information.

.

Computational details

1. Cohesive energy (E_C)

The cohesive energy of the heterostructure (E_{coh}) is calculated using the relation,

$$E_C = \frac{E_{CoP_2/GO} - (N_C E_C + N_{Co} E_{Co} + N_P E_P + N_O E_O + N_H E_H)}{N}$$

Where, $E_{CoP_2/GO}$ is the total energy of CoP_2/GO structure obtained from the ground states structure, E_C,E_{Co},E_P, E_O, and E_H are the energy of the individual atoms found from their stable structure and N_C,N_{Co},N_P,N_O, and N_H is the number of corresponding atoms that are present in the CoP_2/GO structure and N is the total number of atoms.

2. Formation energy (E_F)

The formation energy (E_F) of the CoP_2/GO structure is calculated from the following relation,

$$E_f = E_{CoP_2/GO} - (E_{CoP_2} + E_{GO})$$

Where, $E_{CoP_2/GO}$ is the total energy of CoP_2/GO structure, E_{CoP_2} and E_{GO} are the total energy of the individual CoP_2 and GO structures.

3. Elementary steps of NO_2RR

To study the electrochemical performance, the computational hydrogen electrode (CHE) model proposed Nørskov et al., is adapted [8].

$$H^+_{(aq)} + e^- \rightleftharpoons \frac{1}{2}H_2$$

For the NO_2RR, the reaction occurs via $9e^-$ pathway as given below [9, 10],

$$NO_2^- + 8H^+ + 9e^- \rightarrow NH_3 + H_2O$$

The elementary steps for the reaction are given as,

$$NO_2^- + \ * + e^- \rightarrow NO_2{}^* \tag{S1}$$

$$NO_2{}^* + H^+ + e^- \rightarrow NO_2H^* \tag{S2}$$

$$NO_2H^* + H^+ + e^- \rightarrow NO^* + H_2O \tag{S3}$$

$$NO^* + H^+ + e^- \rightarrow NOH^* \tag{S4}$$

$$NOH^* + H^+ + e^- \rightarrow NHOH^* \tag{S5}$$

$$NHOH^* + H^+ + e^- \rightarrow NH^* + H_2O \tag{S6}$$

$$NOH^* + H^+ + e^- \rightarrow N^* + H_2O \tag{S7}$$

$$N^* + H^+ + e^- \rightarrow NH^* \tag{S8}$$

$$NH^* + H^+ + e^- \rightarrow NH_2{}^* \tag{S9}$$

$$NH_2{}^* + H^+ + e^- \rightarrow NH_3{}^* \tag{S10}$$

$$NH_3^* + H^+ + e^- \rightarrow NH_4^* \qquad \text{(S11)}$$

The Gibbs free energy for the adsorption of the intermediates (NO_2*, NHO_2H*, NOH*, NHOH*, N*, NH*, NH_2*, NH_3*, and NH_4*) and for the reaction steps (S1 – S11) determines the catalytic property materials, which is calculated as,

$$\Delta G = \Delta E + \Delta ZPE - T\Delta S$$

where ΔE is the adsorption energy of the intermediates, ΔZPE and $T\Delta S$ are the change in zero-point energy and entropy at 298.15 K.

4. Faradaic efficiency (FE)

The relation for the Faradaic efficiency (FE) of the NO_2RR is considered from the previous literatures as [10, 11],

$$FE = \left[\frac{1}{1 + exp(\frac{-\Delta G}{K_B T})} \right] \times 100$$

Where, ΔG is the maximum free energy change observed for the reaction steps (S1 – S11), K_B is the Boltzmann constant (8.617×10^{-5} eV K^{-1}), T is the temperature (298.15 K).

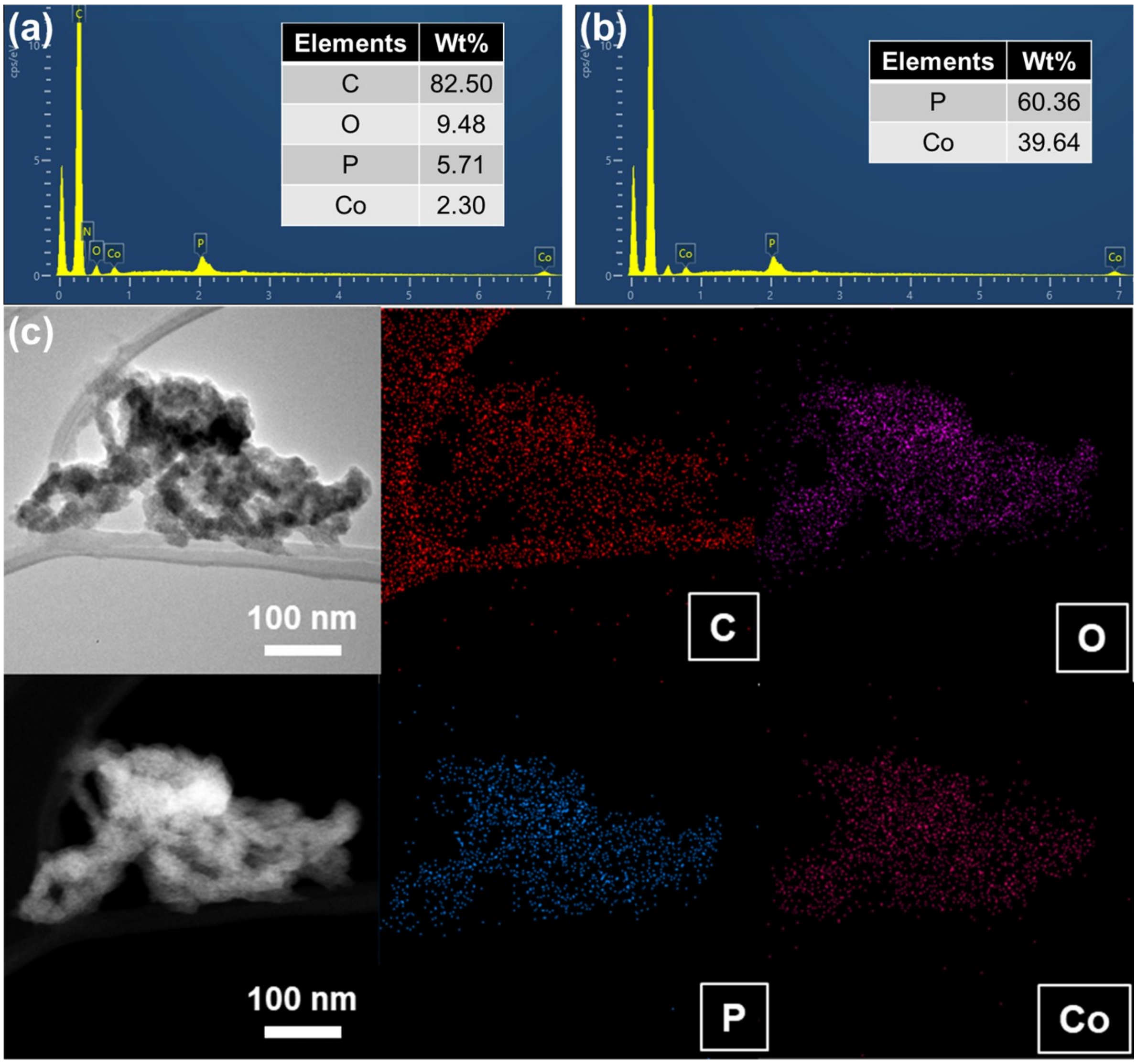

Figure S1. FESEM-EDS spectra of the as-synthesized CoP_2/GO-GF, showing the presence of (a) C, O, P, and Co elements, and (b) P and Co elements without C and O; and (c) TEM studies on CoP_2/GO-GF.

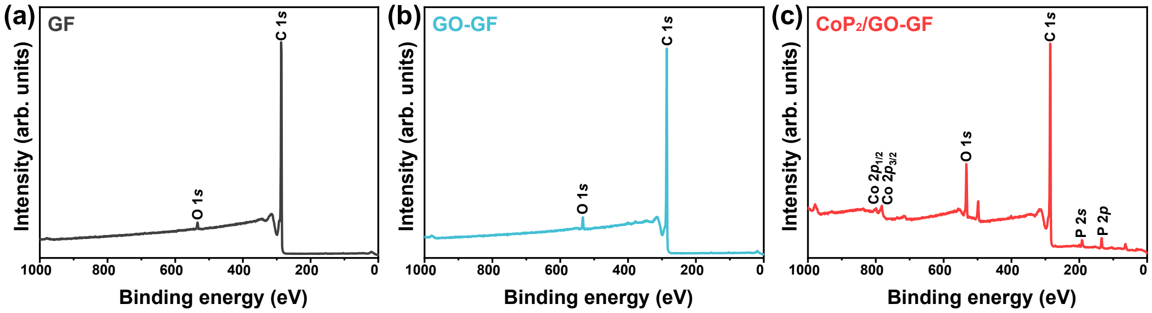

Figure S2. XPS survey spectra of (a) GF, (b) GO-GF, and (c) CoP_2/GO-GF.

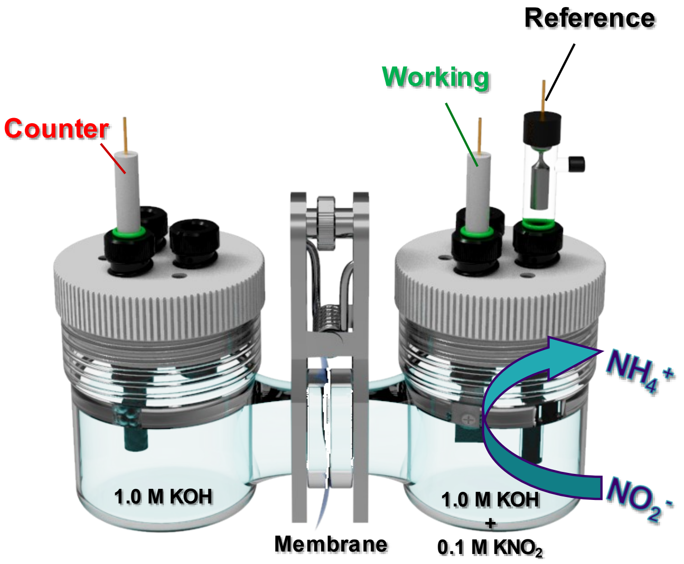

Figure S3. Schematic representation of the two-electrode cell system for NO_2RR.

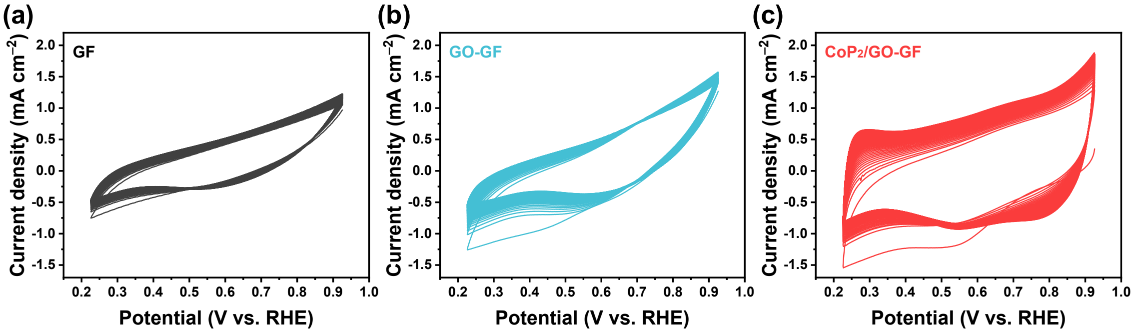

Figure S4. Cyclic voltammograms of (a) GF, (b) GO-GF, and (c) CoP_2/GO-GF.

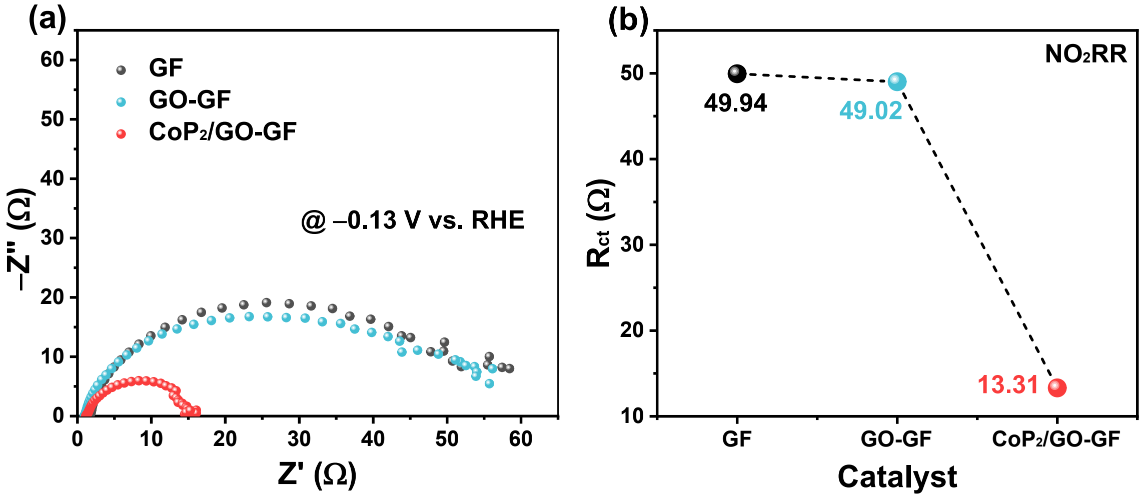

Figure S5. Electrochemical impedance spectroscopy (EIS) analysis of bare GF, GO-GF, and CoP_2/GO-GF at -0.13 V vs. RHE during NO_2RR: (a) Nyquist plots and (b) corresponding charge transfer resistance (R_{ct}) values.

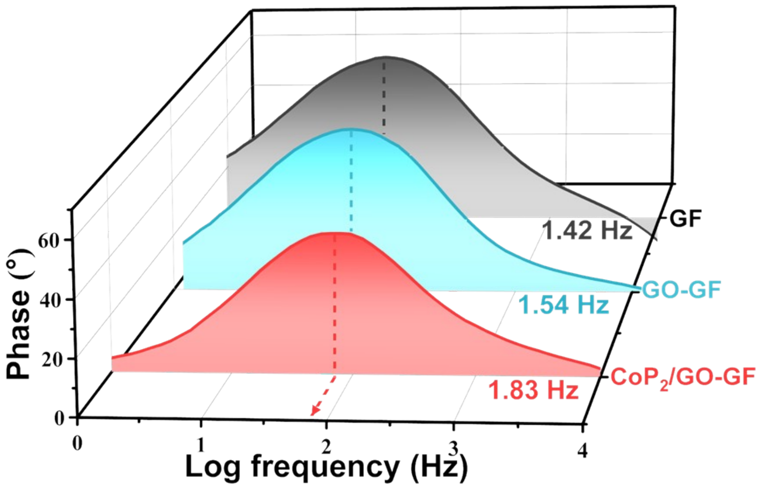

Figure S6. Bode plots of bare GF, GO-GF, and CoP_2/GO-GF at -0.13 V vs. RHE during the NO_2RR.

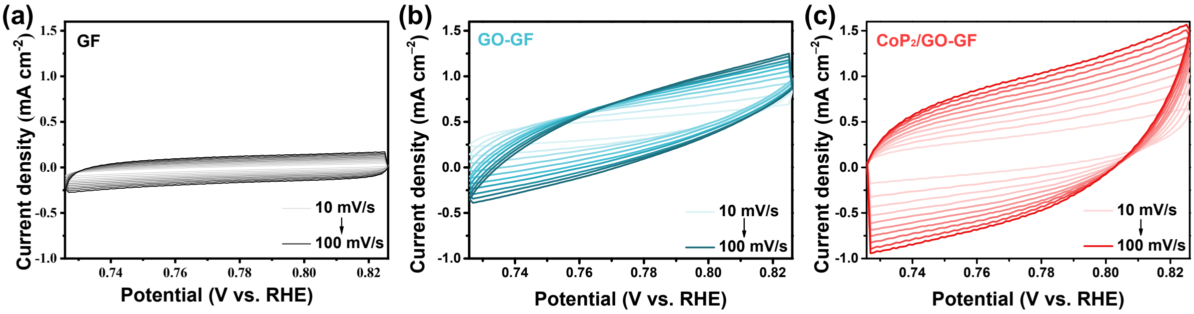

Figure S7. CV curves of (a) bare GF, (b) GO-GF, and (c) CoP_2/ GO-GF samples measured in the non-Faradic portion in 1.0 M KOH + 0.5 M KNO_2 at different scan rates from 10-100 mV s^{-1}.

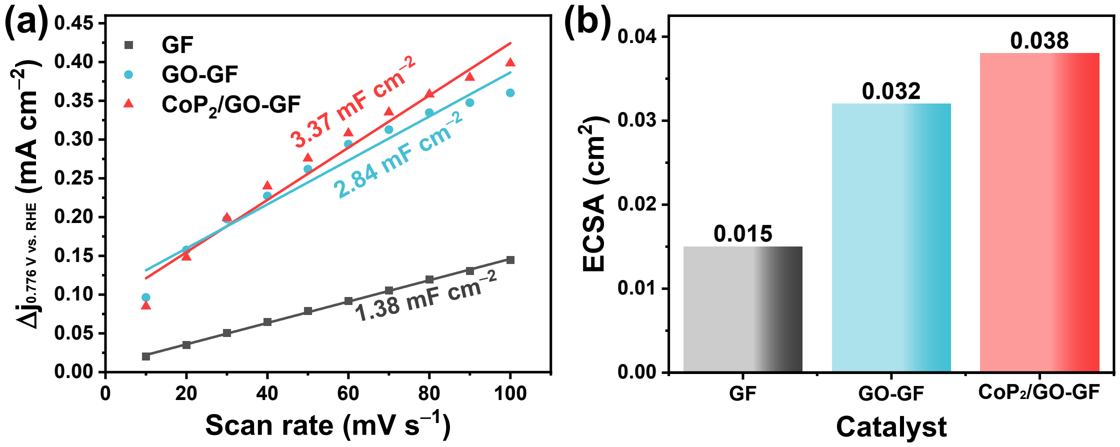

Figure S8. Double-layer capacitance (C_{dl}) and electrochemical surface area (ESCA) of bare GF, GO-GF, and CoP_2/GO-GF studied during the NO_2RR .

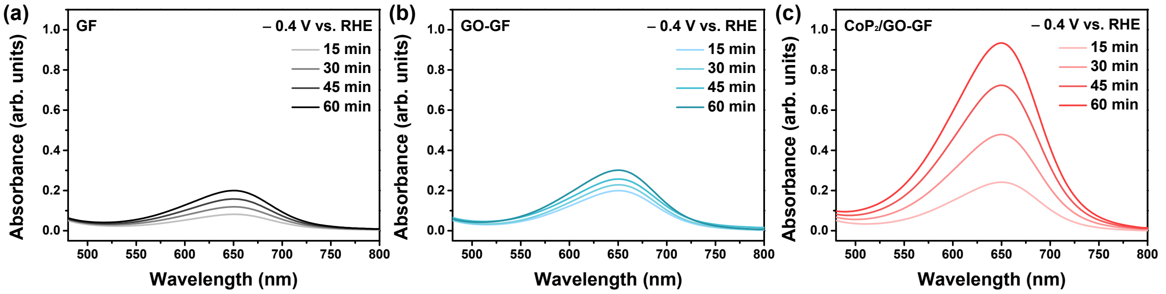

Figure S9. UV-Vis absorption spectra of (a) bare GF, (b) GO-GF, and (c) CoP_2/GO-GF samples measured at -0.4 V vs. RHE.

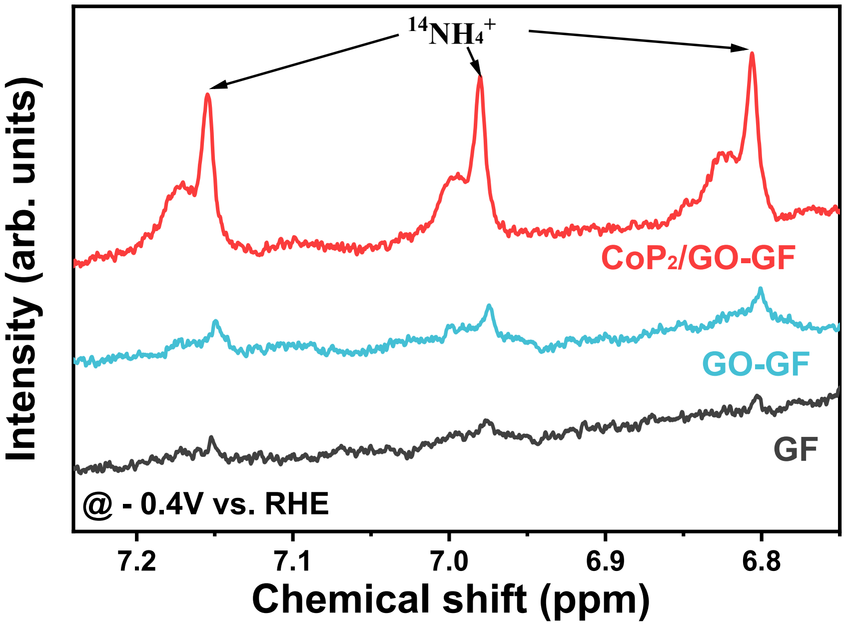

Figure S10. ^{1}H NMR spectra of the catholyte solutions after 60 minutes of NO_2RR over bare GF, GO-GF, and CoP_2/GO-GF at -0.4 V vs. RHE.

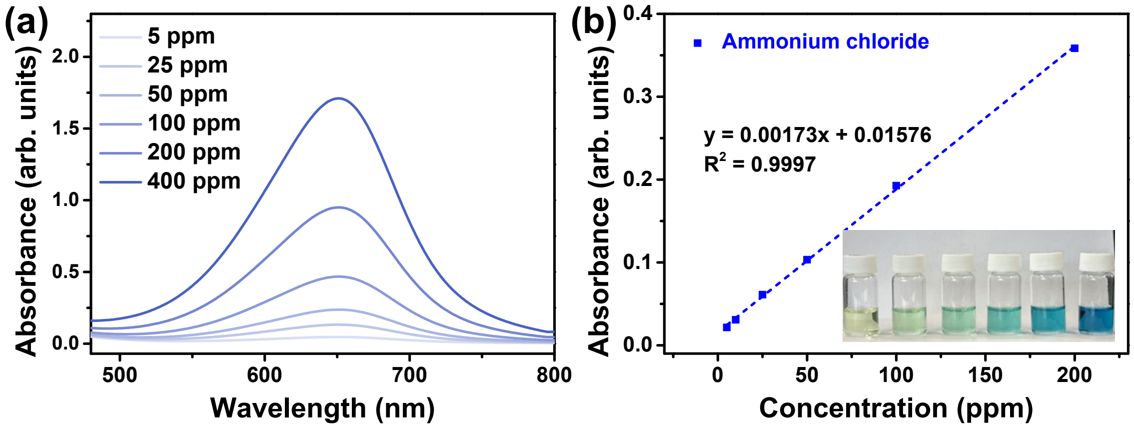

Figure S11. Calibration curves for ammonium ion (NH_4^+) determination: (a) absorbance vs. concentration and (b) linear regression analysis of NH_4Cl standard solutions (5, 10, 25, 50, 100, and 200 ppm).

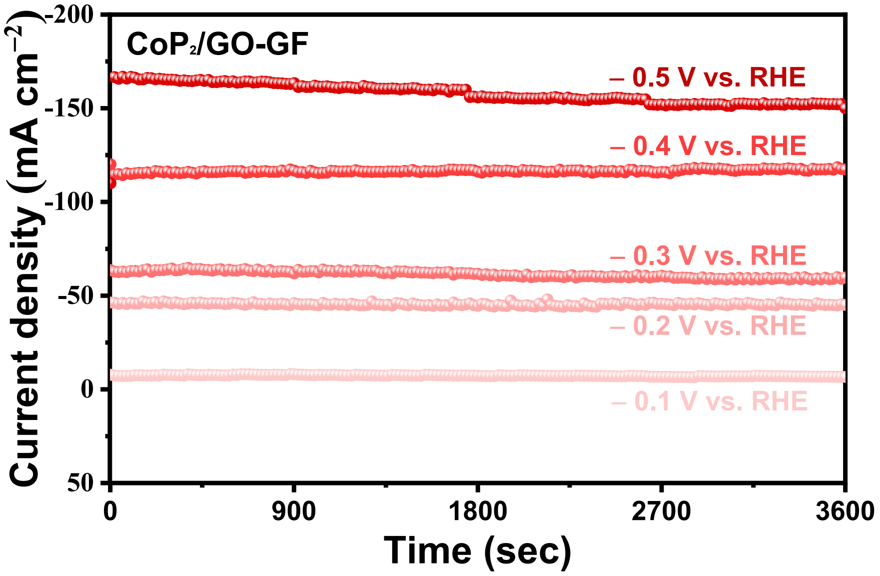

Figure S12. Bulk electrolysis of NO$_2$RR over CoP$_2$/GO-GF samples measured in at potential from 0 to -0.4 V vs. RHE.

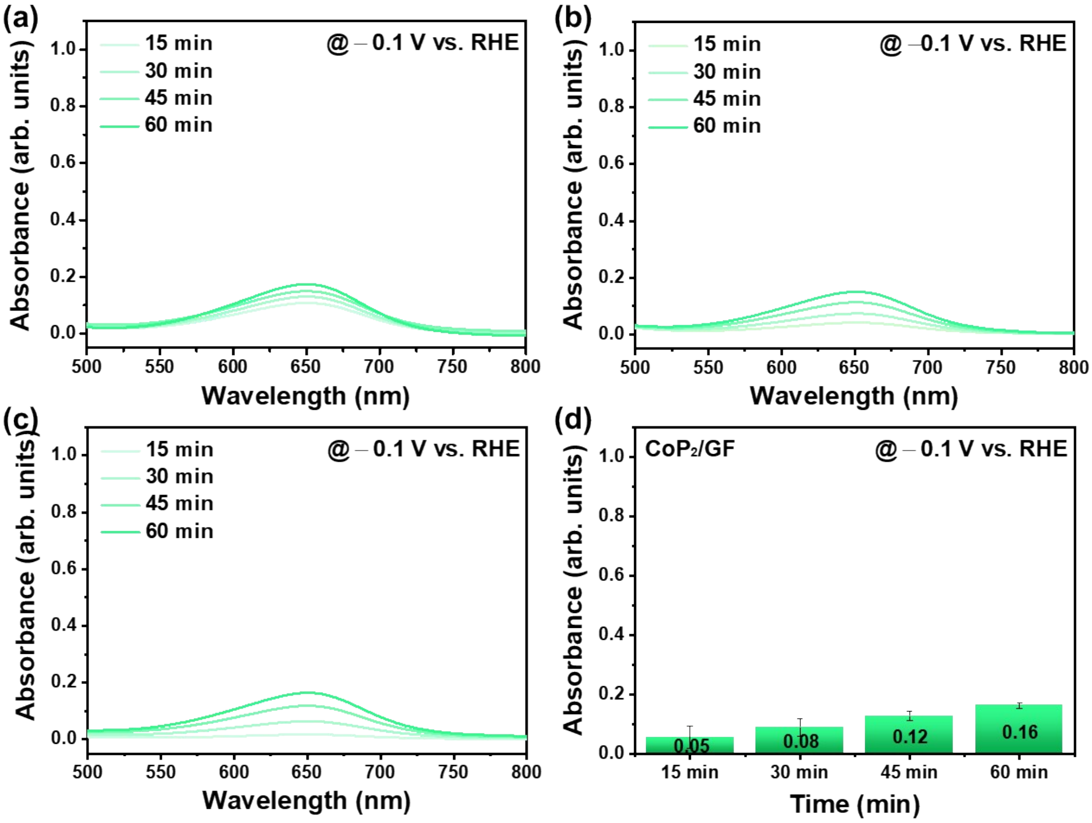

Figure S13. UV-Vis absorption spectra of NH$_4^+$ produced from CoP$_2$/GO-GF samples: (a-c) representative spectra and (d) average absorbance values calculated from three repetitive studies at -0.1 V vs. RHE.

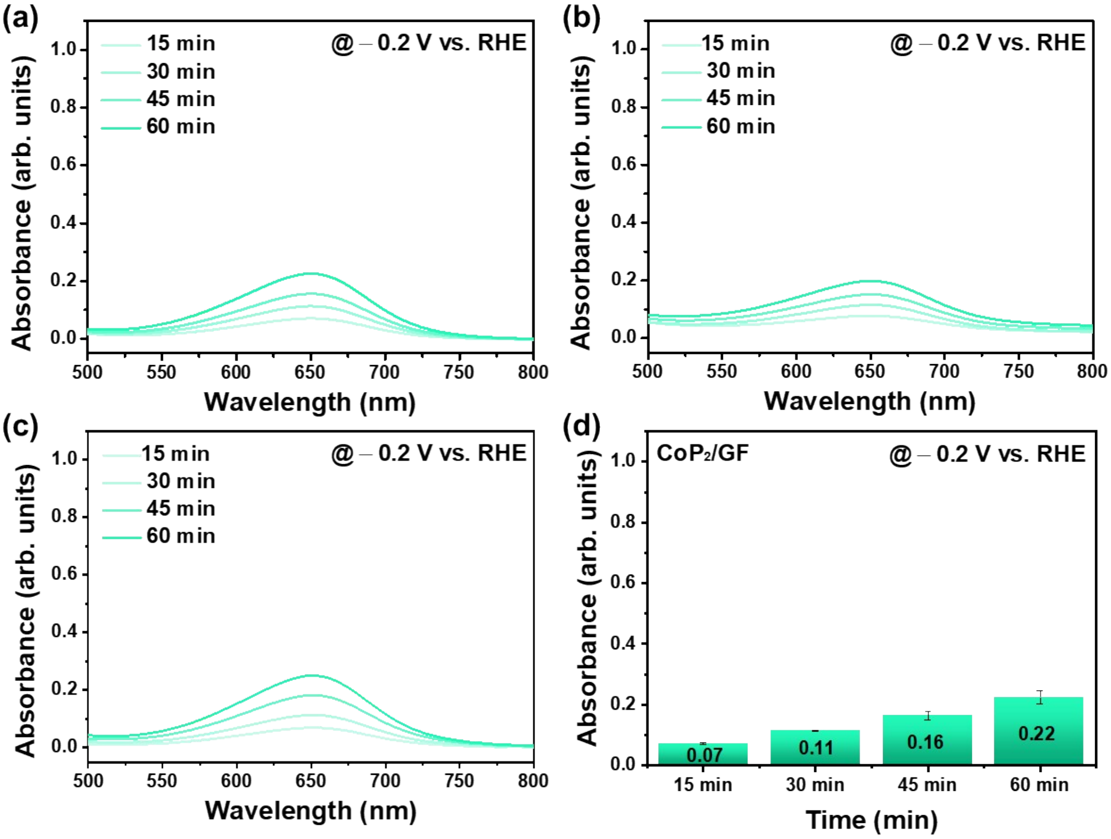

Figure S14. UV-Vis absorption spectra of NH_4^+ produced from CoP_2/GO-GF samples: (a-c) representative spectra and (d) average absorbance values calculated from three repetitive studies at -0.2 V vs. RHE.

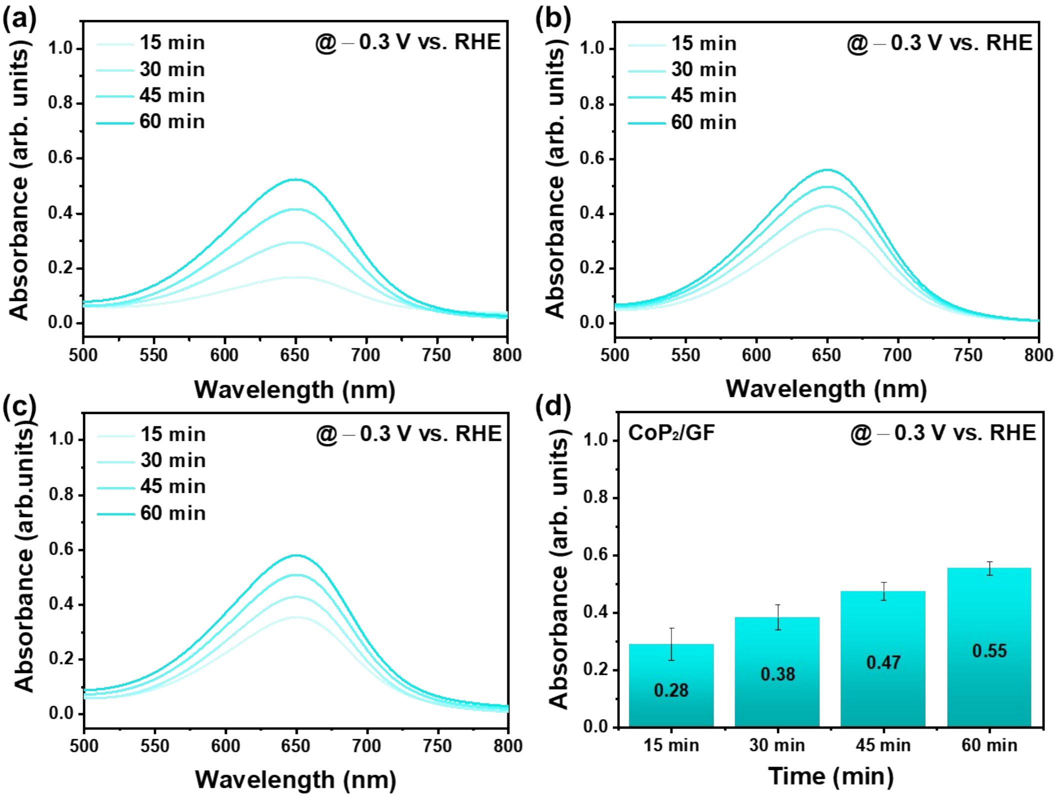

Figure S15. UV-Vis absorption spectra of NH_4^+ produced from CoP_2/GO-GF samples: (a-c) representative spectra and (d) average absorbance values calculated from three repetitive studies at -0.3 V vs. RHE.

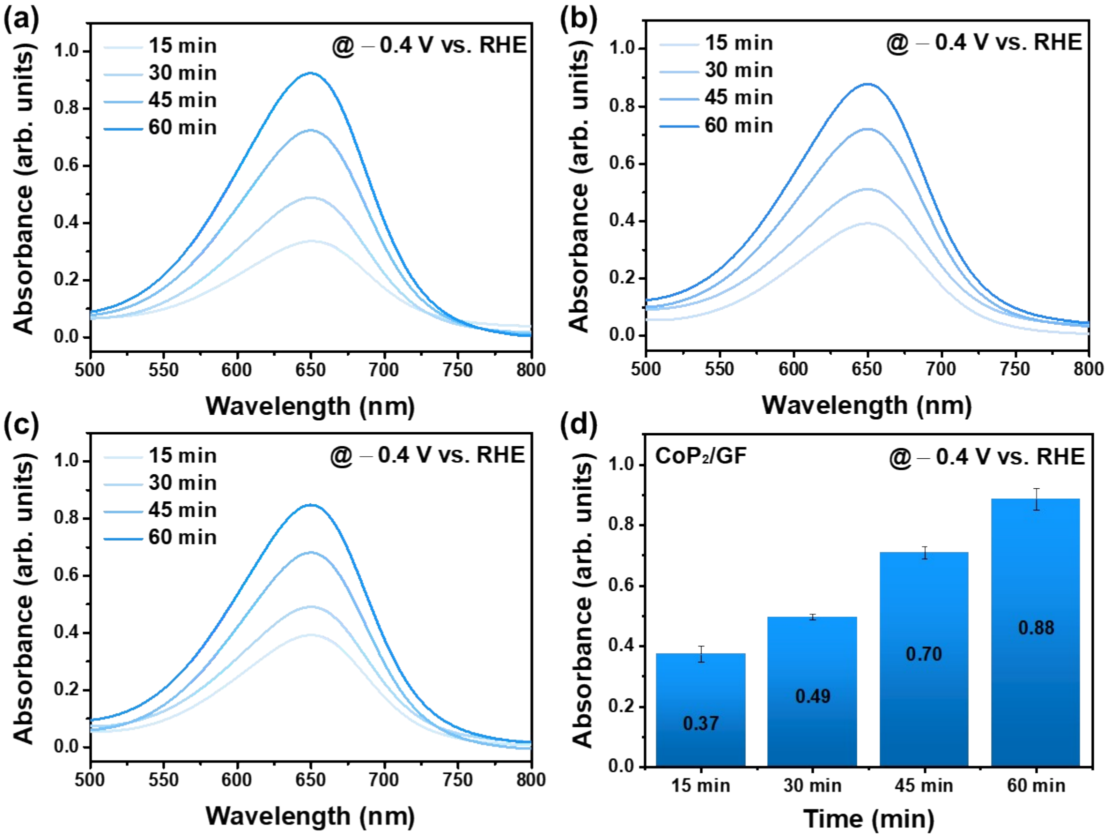

Figure S16. UV-Vis absorption spectra of NH_4^+ produced from CoP_2/GO-GF samples: (a-c) representative spectra and (d) average absorbance values calculated from three repetitive studies at -0.4 V vs. RHE.

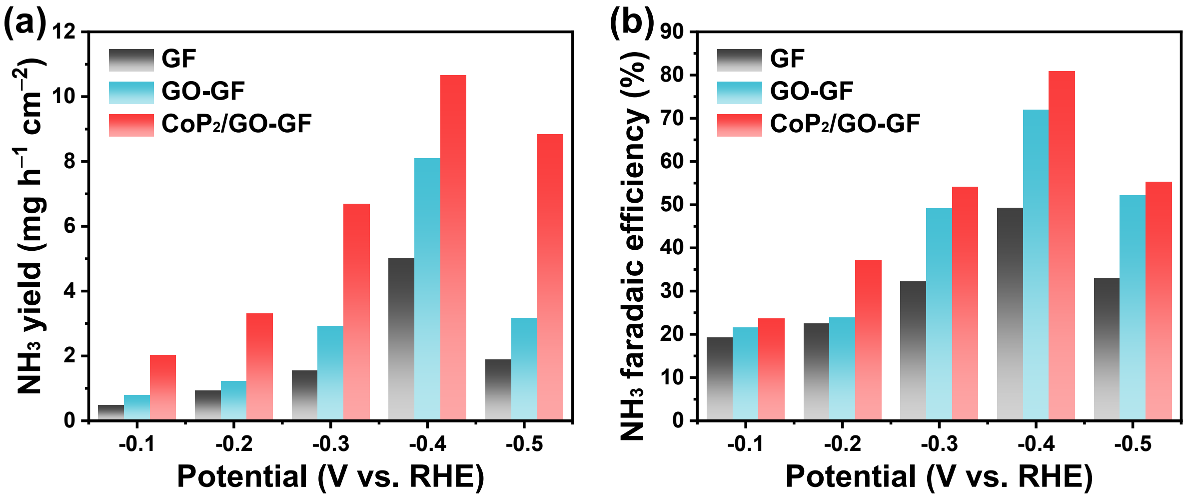

Figure S17. Electrochemical NH_4^+ production over GF, GO-GF, and CoP_2/GO-GF: (a) NH_4^+ yield and (b) NH_4^+ faradaic efficiency calculated from UV-Vis absorption.

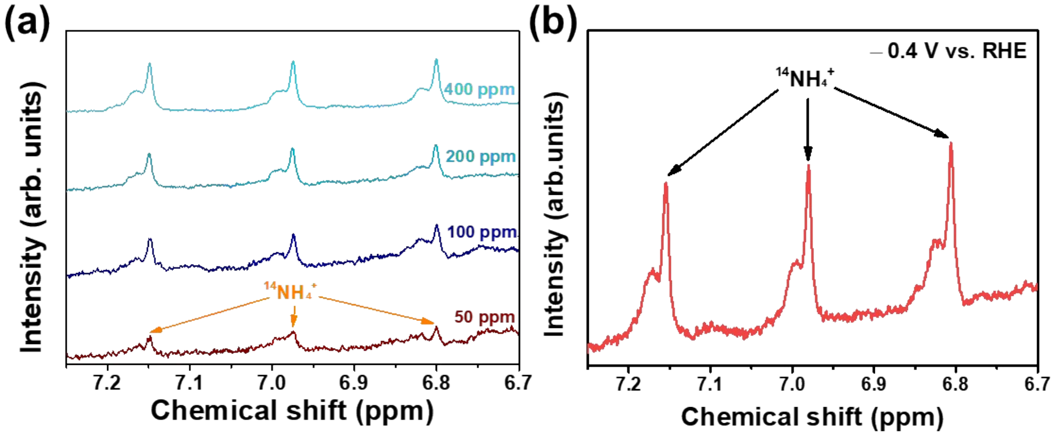

Figure S18. ^{1}H NMR of NH_4^+: (a) calibration spectra for N- NH_4^+ using NH_4Cl standard solutions (50-400 ppm) and (b) ^{1}H NMR spectrum of the catholyte solution after 60 minutes of NO_2RR over CoP_2/GO-GF at -0.4 V vs. RHE.

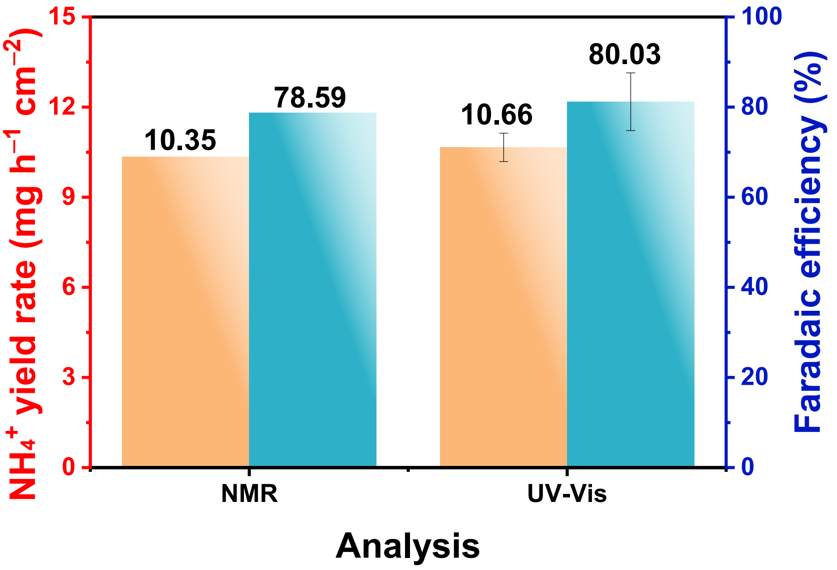

Figure S19. Comparative quantification of N-NH_4^+ by UV-Vis and ^{1}H NMR spectroscopy: NH_4^+ yield and faradaic efficiency for CoP_2/GO-GF.

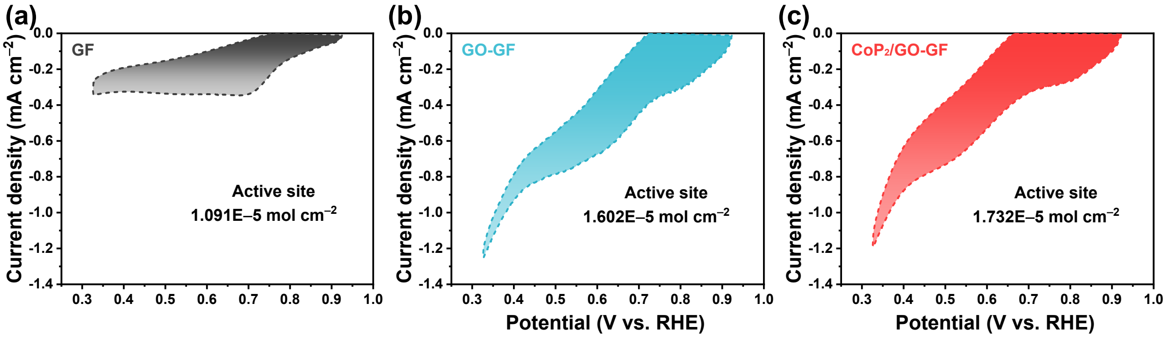

Figure S20. CV curves for (a) bare GF, (b) CO_2 laser GF, and (C) CoP_2/GO-GF, with corresponding active site density values calculated from the CV curves.

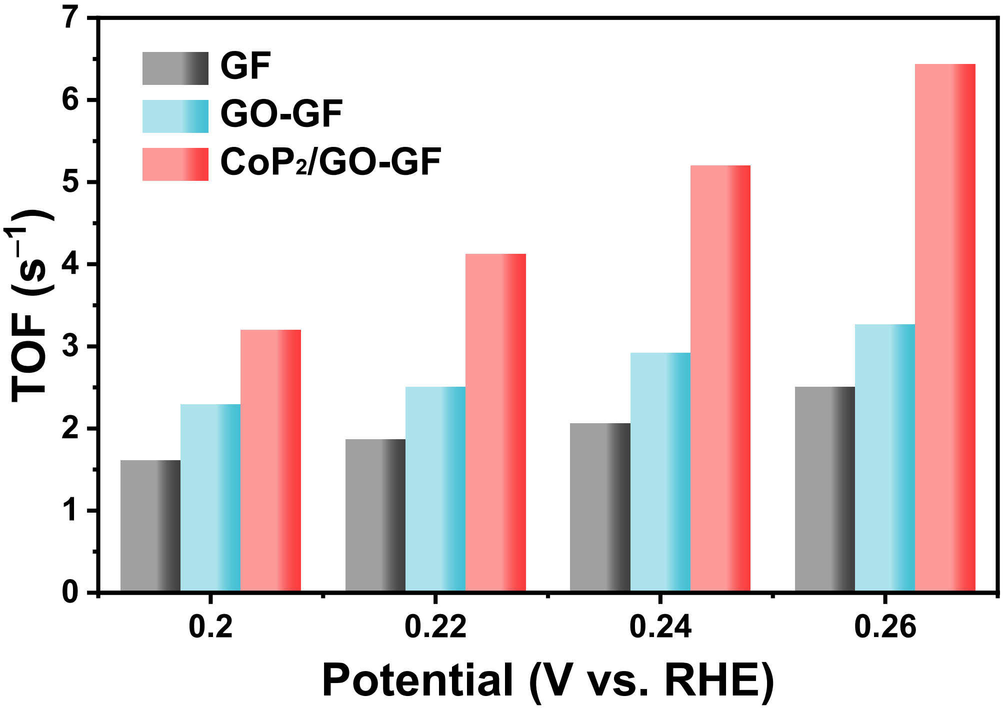

Figure S21. TOF graphs for (a) bare GF, (b) CO_2 laser GF, and (C) CoP_2/GO-GF from NO_2RR.

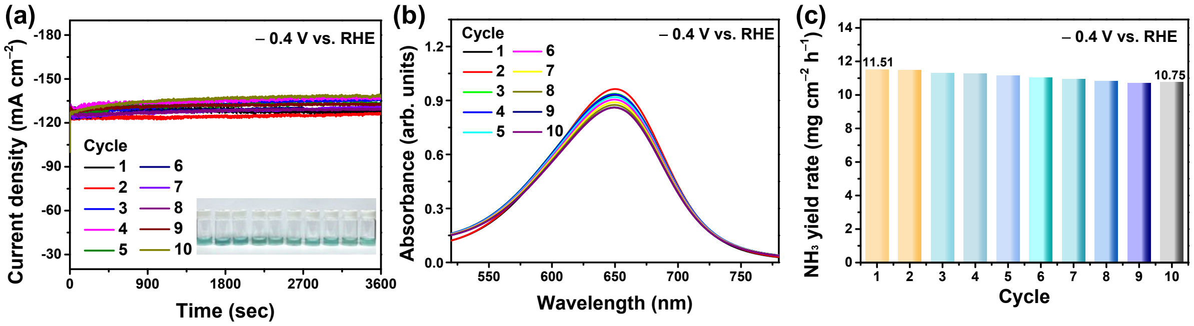

Figure S22. Electrocatalytic stability and performance of CoP_2/GO-GF for NO_2RR: (a) Electrocatalytic stability over 10 consecutive cycles at -0.4 V vs. RHE, with refilling the fresh electrolyte at the start of each cycle, (b) absorption spectra recorded after every 1 hr, and (c) NH_3 yield produced during 10 consecutive cycles of NO_2RR.

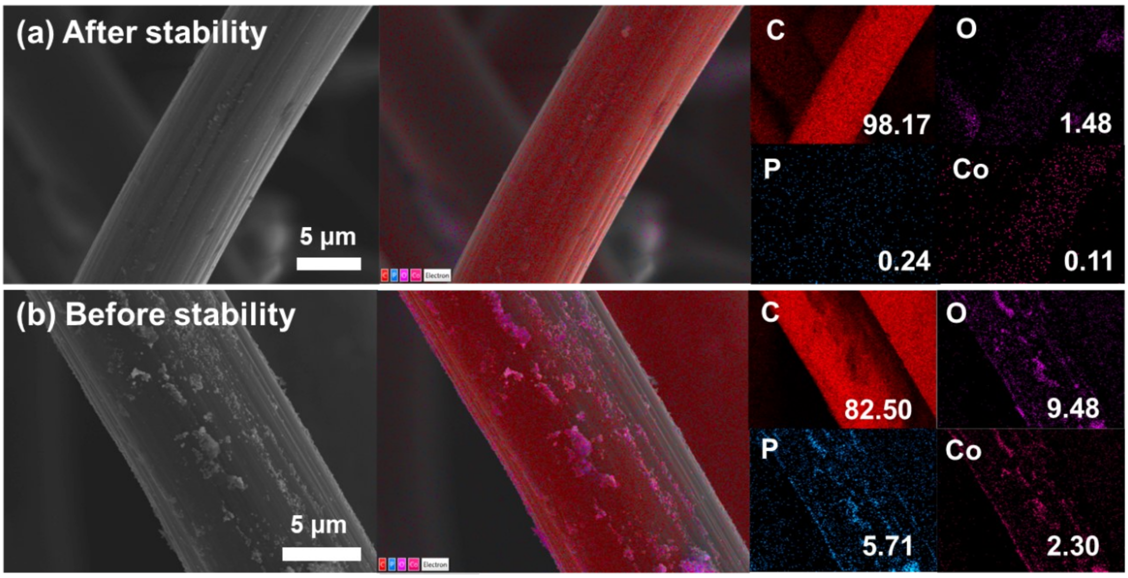

Figure S23. FESEM images and corresponding colour maps of CoP_2/GO-GF: (a) after the NO_2RR stability study, and (b) before the NO_2RR stability study

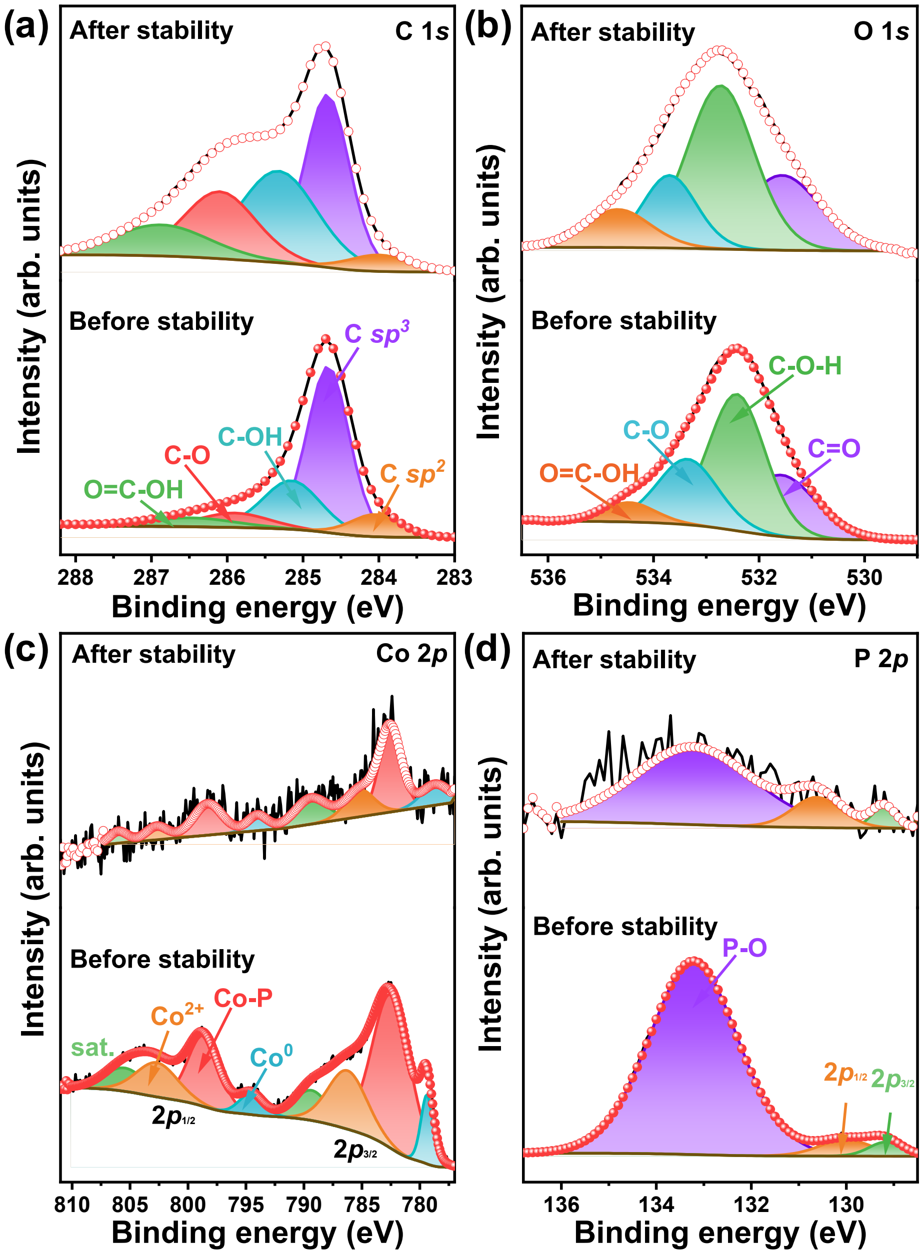

Figure S24. XPS spectra of CoP_2/GO-GF after NO_2RR stability study.

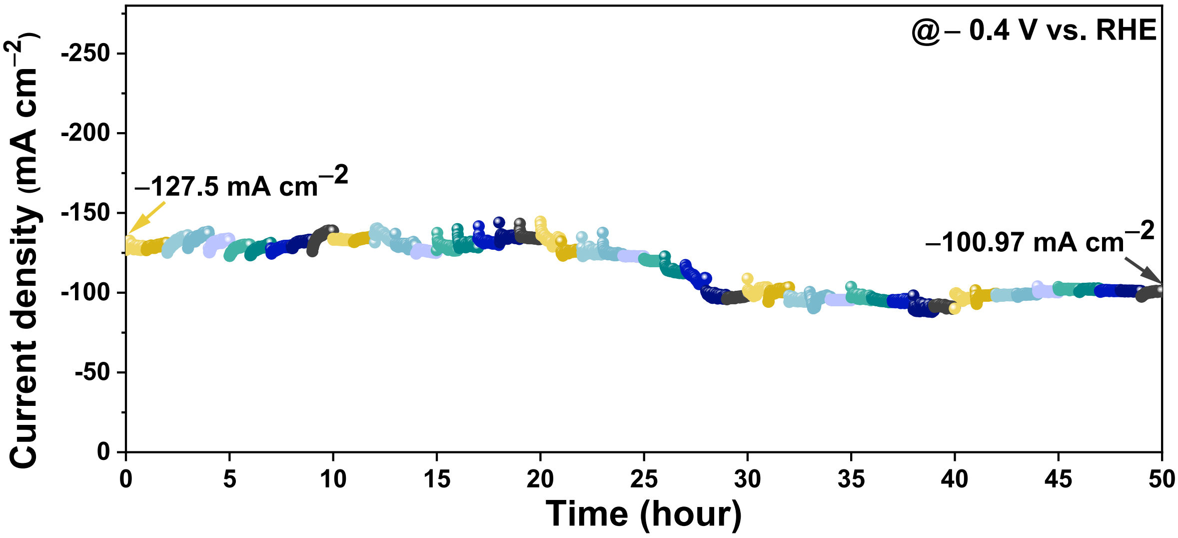

Figure S25. NO_2RR performance on CoP_2/GO-GF for 50 consecutive cycles.

NO_2*	**NO_2H***	**NO***
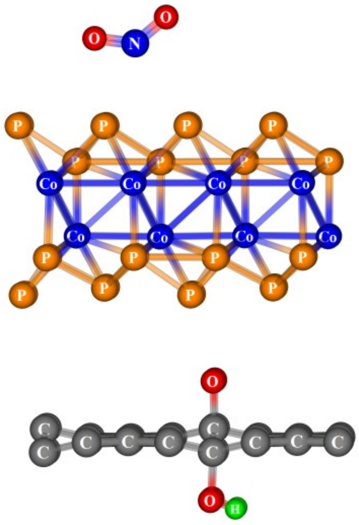	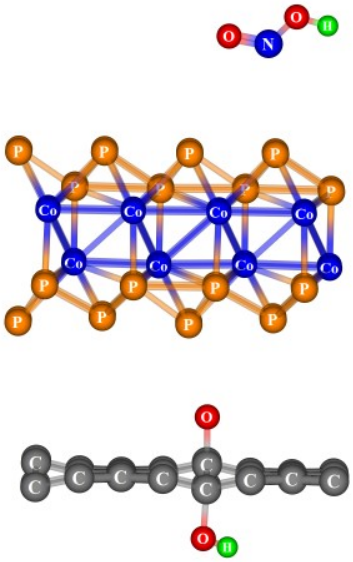	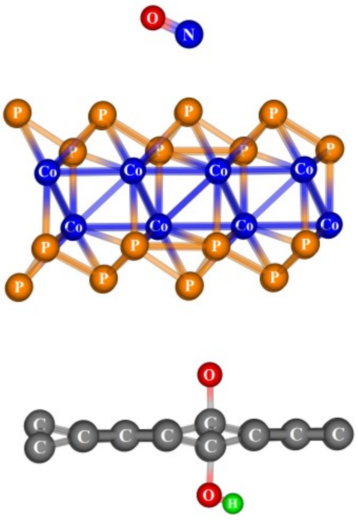
NOH*	**NHOH***	**N***

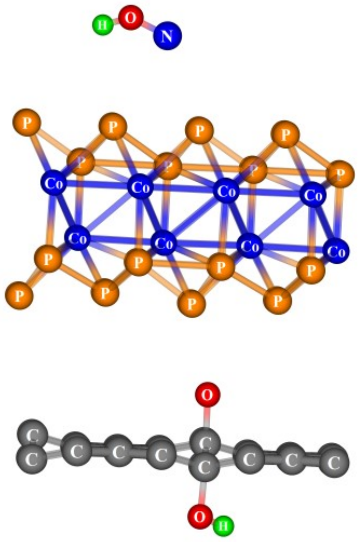	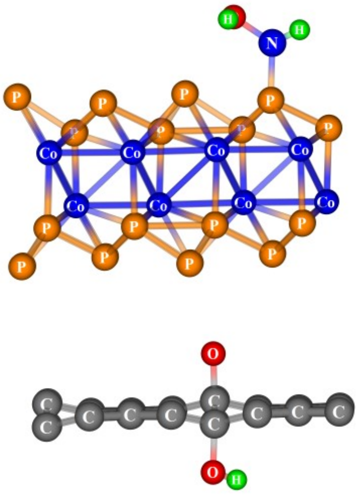	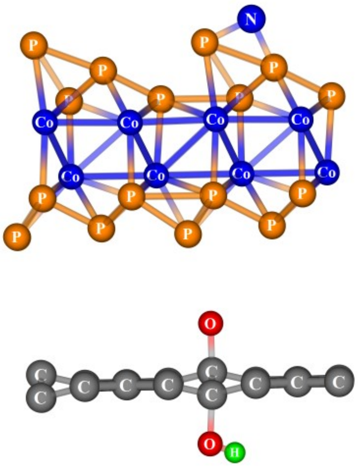
NH*	**NH_2***	**NH_3***
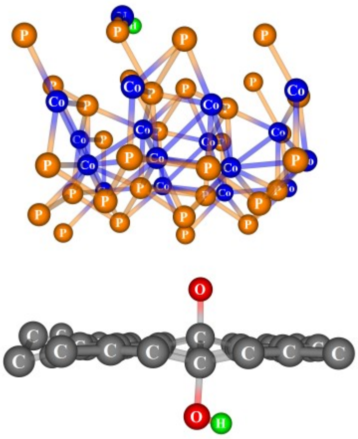	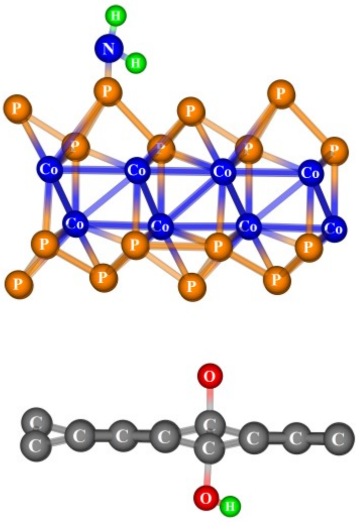	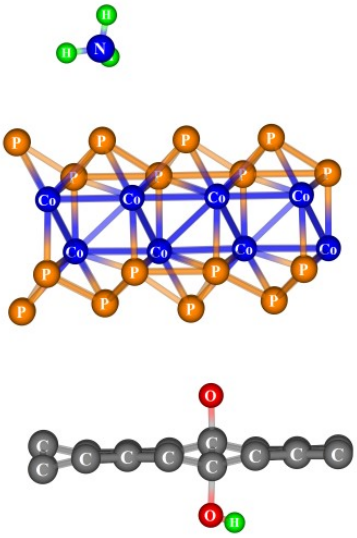
NH_4*		

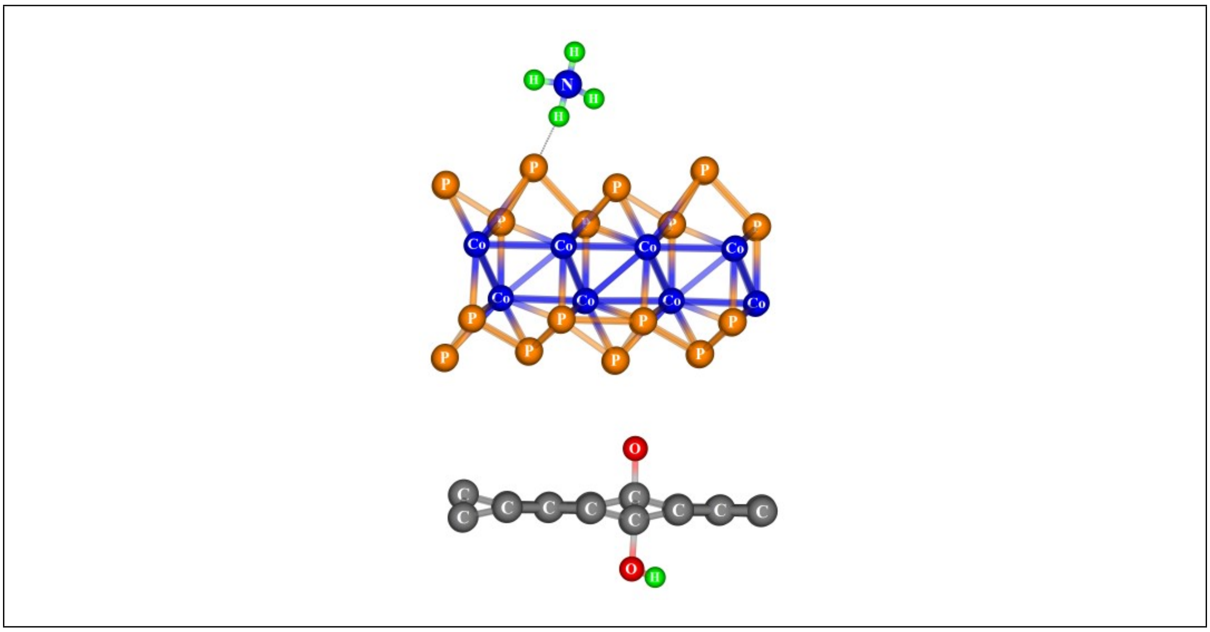

Figure S26. Optimized images of NO_2*, NHO_2H*, NOH*, NHOH*, N*, NH*, NH_2*, NH_3*, and NH_4* intermediates adsorbed structures.

Table S1. Comparison of ammonia yield from the literature studies.

Catalysts	**NH_3 yield**	**Faradaic efficiency**	**Reference**
Ni@MDC	6.3 mg h^{-1}	65.4%	12
CoP-CNS	8.47mmol	88.6%	13
AgNDs	0.6 mg h^{-1}	10.1%	14
O-Cu–PTCDA	0.43 mg h^{-1}	85.9%	15
PCN-NV4	0.00809 mg h^{-1}	11.59%	16
CoP nanoarray/TM	1.4 mg h^{-1}	91.5%	17
Co-10/CNT@CP	19.3 mg h^{-1}	95%	18
BCP	0.28 mg h^{-1}	54.5%	19
Ru SA-NC	12.8 mg h^{-1}	97.8%	20

Fe-PPy SACs	2.75 mg h^{-1}	~100%	[21]
FeSA–N–C	0.00748 mgh^{-1}	56.55%	[22]
Ni-NSA-V_{Ni}	4.0 mg h^{-1}	88.9%	[23]
CoP NA/TM	2.3 mg h^{-1}	90%	[24]
MoFe protein	234 nmol (30min)	~100%	[25]
CoB@TiO_2/TP	233.1 μmol h^{-1}	95.2%	[26]
$Ti_3C_2T_x$	0.65 mg h^{-1}	75%	[27]
Cu_3P NA/CF	~95 μmol h^{-1}	~91%	[28]
Fe-SAC	20 mg h^{-1}	75%	[29]
CoP_2/GO-GF	10.3 mg h^{-1}	~78%	This work

Reference

1. G. Kresse and D. Joubert, *Physical Review B*, 1999, **59**, 1758-1775.
2. G. Kresse and J. Furthmüller, *Physical Review B*, 1996, **54**, 11169-11186.
3. J. P. Perdew, K. Burke and M. Ernzerhof, *Physical Review Letters*, 1996, **77**, 3865-3868.
4. P. E. Blöchl, *Physical Review B*, 1994, **50**, 17953-17979.
5. S. Grimme, S. Ehrlich and L. Goerigk, *Journal of Computational Chemistry*, 2011, **32**, 1456-1465.
6. H. J. Monkhorst and J. D. Pack, *Physical Review B*, 1976, **13**, 5188-5192.
7. P. E. Blöchl, O. Jepsen and O. K. Andersen, *Physical Review B*, 1994, **49**, 16223-16233.
8. J. K. Nørskov, T. Bligaard, A. Logadottir, J. R. Kitchin, J. G. Chen, S. Pandelov and U. Stimming, *Journal of The Electrochemical Society*, 2005, **152**, J23.
9. P. Lv, D. Wu, B. He, X. Li, R. Zhu, G. Tang, Z. Lu, D. Ma and Y. Jia, *Journal of Materials Chemistry A*, 2022, **10**, 9707-9716.

10. K. Yang, S.-H. Han, C. Cheng, C. Guo, T. Li and Y. Yu, *Journal of the American Chemical Society*, 2024, **146**, 12976-12983.
11. N. Sathishkumar, S.-Y. Wu and H.-T. Chen, *Applied Surface Science*, 2022, **598**, 153829.
12. X. He, X. Li, X. Fan, J. Li, D. Zhao, L. Zhang, S. Sun, Y. Luo, D. Zheng, L. Xie, A. M. Asiri, Q. Liu and X. Sun, *ACS Applied Nano Materials*, 2022, **5**, 14246-14250.
13. K. Fan, W. Xie, J. Li, Y. Sun, P. Xu, Y. Tang, Z. Li and M. Shao, *Nature Communications*, 2022, **13**, 7958.
14. W. Li, K. Li, Y. Ye, S. Zhang, Y. Liu, G. Wang, C. Liang, H. Zhang and H. Zhao, *Communications Chemistry*, 2021, **4**, 10.
15. G.-F. Chen, Y. Yuan, H. Jiang, S.-Y. Ren, L.-X. Ding, L. Ma, T. Wu, J. Lu and H. Wang, *Nature Energy*, 2020, **5**, 605-613.
16. C. Lv, Y. Qian, C. Yan, Y. Ding, Y. Liu, G. Chen and G. Yu, *Angewandte Chemie International Edition*, 2018, **57**, 10246-10250.
17. X. Fan, L. Xie, J. Liang, Y. Ren, L. Zhang, L. Yue, T. Li, Y. Luo, N. Li, B. Tang, Y. Liu, S. Gao, A. A. Alshehri, Q. Liu, Q. Kong and X. Sun, *Nano Research*, 2022, **15**, 3050-3055.
18. S.-L. Meng, C. Zhang, C. Ye, J.-H. Li, S. Zhou, L. Zhu, X.-B. Li, C.-H. Tung and L.-Z. Wu, *Energy & Environmental Science*, 2023, **16**, 1590-1596.
19. S. Liu, T. Qian, M. Wang, H. Ji, X. Shen, C. Wang and C. Yan, *Nature Catalysis*, 2021, **4**, 322-331.
20. Z. Ke, D. He, X. Yan, W. Hu, N. Williams, H. Kang, X. Pan, J. Huang, J. Gu and X. Xiao, *ACS Nano*, 2023, **17**, 3483-3491.
21. P. Li, Z. Jin, Z. Fang and G. Yu, *Energy & Environmental Science*, 2021, **14**, 3522-3531.
22. M. Wang, S. Liu, T. Qian, J. Liu, J. Zhou, H. Ji, J. Xiong, J. Zhong and C. Yan, *Nature Communications*, 2019, **10**, 341.
23. C. Wang, W. Zhou, Z. Sun, Y. Wang, B. Zhang and Y. Yu, *Journal of Materials*

Chemistry A, 2021, **9**, 239-243.

24. G. Wen, J. Liang, Q. Liu, T. Li, X. An, F. Zhang, A. A. Alshehri, K. A. Alzahrani, Y. Luo, Q. Kong and X. Sun, *Nano Research*, 2022, **15**, 972-977.
25. R. D. Milton, S. Abdellaoui, N. Khadka, D. R. Dean, D. Leech, L. C. Seefeldt and S. D. Minteer, *Energy & Environmental Science*, 2016, **9**, 2550-2554.
26. L. Hu, D. Zhao, C. Liu, Y. Liang, D. Zheng, S. Sun, Q. Li, Q. Liu, Y. Luo, Y. Liao, L. Xie and X. Sun, *Inorganic Chemistry Frontiers*, 2022, **9**, 6075-6079.
27. R. Nittoor-Veedu, X. Ju, M. Langer, W. Gao, M. Otyepka and M. Pumera, *Small*, 2025, **21**, 2410105.
28. J. Liang, B. Deng, Q. Liu, G. Wen, Q. Liu, T. Li, Y. Luo, A. A. Alshehri, K. A. Alzahrani, D. Ma and X. Sun, *Green Chemistry*, 2021, **23**, 5487-5493.
29. Z.-Y. Wu, M. Karamad, X. Yong, Q. Huang, D. A. Cullen, P. Zhu, C. Xia, Q. Xiao, M. Shakouri, F.-Y. Chen, J. Y. Kim, Y. Xia, K. Heck, Y. Hu, M. S. Wong, Q. Li, I. Gates, S. Siahrostami and H. Wang, *Nature Communications*, 2021, **12**, 2870.